

Constructing Chromium Multioxide Hole-Selective Heterojunction for High-Performance Perovskite Solar Cells

Sheng Jiang, Shaobing Xiong, Wei Dong, Danqin Li, Yuting Yan, Menghui Jia, Yannan Dai, Qingbiao Zhao, Kai Jiang,* Xianjie Liu, Liming Ding,* Mats Fahlman, Zhenrong Sun, and Qinye Bao*

Perovskite solar cells (PSCs) suffer from significant nonradiative recombination at perovskite/charge transport layer heterojunction, seriously limiting their power conversion efficiencies. Herein, solution-processed chromium multioxide (CrO_x) is judiciously selected to construct a $\text{MAPbI}_3/\text{CrO}_x/\text{Spiro-OMeTAD}$ hole-selective heterojunction. It is demonstrated that the inserted CrO_x not only effectively reduces defect sites via redox shuttle at perovskite contact, but also decreases valence band maximum (VBM)-HOMO offset between perovskite and Spiro-OMeTAD. This will diminish thermionic losses for collecting holes and thus promote charge transport across the heterojunction, suppressing both defect-assisted recombination and interface carrier recombination. As a result, a remarkable improvement of 21.21% efficiency with excellent device stability is achieved compared to 18.46% of the control device, which is among the highest efficiencies for polycrystalline MAPbI_3 based n-i-p planar PSCs reported to date. These findings of this work provide new insights into novel charge-selective heterojunctions for further enhancing efficiency and stability of PSCs.

next-generation photovoltaic absorbers due to their superior optoelectronic properties including large absorption coefficients,^[1–3] small exciton binding energies,^[4,5] and high carrier mobilities.^[6–8] Attributed to worldwide research efforts recently, the past decade has featured a fantastic growth rate in the power conversion efficiency (PCE) of single-junction perovskite solar cells (PSCs) from 3.8%^[9] to a certified 25.7%^[10] which approaches the efficiencies of state-of-the-art crystalline silicon solar cells. However, the “imperfect contact” between the perovskite and charge transport layers within PSCs seriously limits further improvement in both efficiency output and operational stability.^[11,12] It is well established that polycrystalline perovskite films inevitably suffer from tremendous defects on the film surface,^[13] which cause nonradiative recombination of photogenerated carriers and Fermi level pinning at interface.^[14–16] Moreover, the interface energetics at the contact have a very important influence

on the device performance, especially in terms of photovoltage.^[17] The relative positions of perovskite's valence or conduction bands and charge transport layer's frontier energy

1. Introduction

Organic–inorganic halide perovskite semiconductors have received much attention as one of the most auspicious

S. Jiang, S. Xiong, D. Li, Y. Yan, Y. Dai, Q. Zhao, K. Jiang, Q. Bao
School of Physics and Electronic Science
East China Normal University
Shanghai 200241, China
E-mail: kjiang@ee.ecnu.edu.cn; qybao@clpm.ecnu.edu.cn


W. Dong
Shanghai Key Laboratory of Magnetic Resonance
East China Normal University
Shanghai 200241, China

M. Jia, Z. Sun
State Key Laboratory of Precision Spectroscopy
East China Normal University
Shanghai 200241, China

X. Liu, M. Fahlman
Laboratory of Organic Electronics, ITN
Linköping University
Norrköping SE-60174, Sweden

L. Ding
Center for Excellence in Nanoscience (CAS), Key Laboratory of
Nanosystem and Hierarchical Fabrication (CAS)
National Center for Nanoscience and Technology
Beijing 100190, China
E-mail: ding@nanocr.cn

Q. Bao
Collaborative Innovation Center of Extreme Optics
Shanxi University
Taiyuan, Shanxi 030006, China

 The ORCID identification number(s) for the author(s) of this article can be found under <https://doi.org/10.1002/advs.202203681>

© 2022 The Authors. Advanced Science published by Wiley-VCH GmbH. This is an open access article under the terms of the Creative Commons Attribution License, which permits use, distribution and reproduction in any medium, provided the original work is properly cited.

DOI: 10.1002/advs.202203681

levels, i.e., highest occupied molecular orbital (HOMO) or lowest unoccupied molecular orbital (LUMO) levels, significantly determine charge transport across the interface.^[18,19] Therefore, constructing optimized charge-selective heterojunction with reduced defects and matched energetics will be crucial to further improve the performance of PSCs.

The solid-state 2, 2', 7, 7'-Tetrakis[*N,N*-di(4-methoxyphenyl)amino]-9, 9'-spirobifluorene (Spiro-OMeTAD) is the most widely used hole transport layer in high-performance PSCs with *n-i-p* configuration.^[20,21] However, the existence of a large energy level offset between perovskite's valence band maximum (VBM) and Spiro-OMeTAD's HOMO constrains the built-in field and leads to thermionic loss for the collected holes at the heterojunction in the PSCs.^[22–26] Furthermore, the penetrative iodine ions (I[−]) can chemically interact with Spiro-OMeTAD⁺ and deteriorate the long-term maintenance of the device performance.^[27] Strategies of inserting an interlayer to modify the heterojunction between the perovskite and charge transport layers hence is highly desirable to boost optoelectronic properties of PSCs.^[28–30]

In this work, we demonstrate a highly efficient hole-selective heterojunction in the *n-i-p* planar PSCs, wherein a solution-processed chromium multioxide (CrO_x) interlayer is introduced between the perovskite and Spiro-OMeTAD. Metal oxides are superior in terms of conductivity, wide band gap, and stability than conjugated small molecule and polymers.^[31–34] The multivalence state oxides CrO_x simultaneously reduce defect sites via redox shuttle at perovskite contact, and decrease the VBM-HOMO energy offset between the perovskite and Spiro-OMeTAD to diminish thermionic losses for collecting holes and to promote charge transport at the perovskite/CrO_x/Spiro-OMeTAD heterojunction, resulting in the suppression of both defect-assisted recombination and interface carrier recombination in the PSCs. As a result, we achieve a remarkably improved PCE of 21.21% compared to 18.46% of the control device. It is among the highest efficiencies for polycrystalline MAPbI₃ based *n-i-p* planar PSCs reported to date. Moreover, the device stability is significantly enhanced due to the stabilization effects at the heterojunction. The unencapsulated device maintains 90% of its initial efficiency after as long as 500 h storage in 60% relative humidity at room temperature under air, whereas the control device can remain only 10% of its initial efficiency. At such heterojunction, the CrO_x enhances the hole transport, avoids the hole accumulation, and impedes the attack of moisture on the perovskite film and the iodine ion migration into the Spiro-OMeTAD layer. This work highlights a promising strategy of constructing a highly effective charge-selective heterojunction to further increase efficiency and stability of PSCs.

2. Results and Discussion

Figure 1a presents the fabrication process of a MAPbI₃/CrO_x/Spiro-OMeTAD hole-selective heterojunction. Detailed film preparations are given in the Experimental Section. X-ray photoelectron spectroscopy (XPS) is applied to confirm the successful insertion of CrO₃ thin layer between the perovskite and Spiro-OMeTAD. The deconvolution of XPS Cr 2p_{3/2} core level spectrum by Gaussian–Lorentzian line shapes demonstrates that the solution-processed CrO_x film in fact composes multivalence state oxide complexes including CrO₃, Cr(OH)₃,

Cr₂O₃, and CrO₂ (Figure 1b), where the Cr(OH)₃ constituent originates from hydroxylation in the isopropanol solution.^[35] The ion pair Cr⁶⁺ – Cr³⁺ (Cr⁴⁺) can function as a redox shuttle that oxidizes Pb⁰ and reduces I⁰ defects via the chemical reactions of Cr⁶⁺ + Pb⁰ → Pb²⁺ + Cr₃ + (Cr⁴⁺), and Cr³⁺ (Cr⁴⁺) + I⁰ → Cr⁶⁺ + I[−] at the perovskite/CrO_x interface.^[36] We then carry out UV photoelectron spectroscopy (UPS) measurement to investigate the interfacial energetics of the MAPbI₃/CrO_x/Spiro-OMeTAD heterojunction (Figure 1c,d). Determined from these UPS spectra, the VBM of MAPbI₃ and the HOMO of Spiro-OMeTAD with respect to the Fermi level (*E*_F) position are 1.28 and 0.88 eV, respectively. It clearly indicates that there is a 0.4 eV VBM-HOMO energy offset (Figure 1e), which in principle constrains the built-in field and thus leads to thermionic losses for collecting holes at the MAPbI₃/Spiro-OMeTAD interface. After inserting a thin CrO_x layer, the VBM of the CrO_x is located at 1.08 eV below the *E*_F (Figure 1f), creating a step-type energy level alignment at the MAPbI₃/CrO_x/Spiro-OMeTAD heterojunction. Such energy level alignment effectively can reduce the thermionic losses for the holes and promote hole transport from MAPbI₃ to Spiro-OMeTAD. Considering that the work function of MAPbI₃/CrO_x film (4.45 eV) is same as that of the pristine MAPbI₃ confirmed by no energy shift of XPS Pb 4f, I 3d and N 1s core level spectra (Figure S1, Supporting Information), we hence conclude that there is no potential step at the perovskite/CrO_x interface. This is different from the case of perovskite/thermal-evaporated molybdenum trioxide interface with the formation of an interface dipole as reported previously.^[37] Correspondingly, the intrinsic work function of the solution-processed CrO_x film is also 4.45 eV (Figure S2, Supporting Information). Figure 1g shows the surface atomic force microscopy (AFM) measurements of the perovskite films, where the root mean square (RMS) roughness reduces from 10.9 (MAPbI₃) to 7.2 nm (MAPbI₃/CrO_x), and the surface height histogram of the MAPbI₃/CrO_x film exhibits a clear shift toward lower heights, i.e., a smoother surface (Figure 1h). It is believed that a smoother surface is one of the key reasons for improving charge transport at the MAPbI₃/CrO_x/Spiro-OMeTAD heterojunction.^[38]

Figure 2a displays the UV-vis absorption spectra of the MAPbI₃ and MAPbI₃/CrO_x films. The MAPbI₃/CrO_x film has a slight enhancement of the optical absorbance owing to defect reduction at the interface. The unchanged intensities of X-ray diffraction (XRD) patterns demonstrate that the solution-processed CrO_x does not influence the perovskite film crystallinity (Figure S3, Supporting Information). We further perform steady-state photoluminescence (PL) and time-resolved photoluminescence (TRPL) to probe the charge dynamics. When compared to the perovskite films without a charge transport layer, the increased PL intensity (Figure 2b) provides evidence that CrO_x helps to suppress nonradiative recombination by eliminating perovskite surface defect sites, which is consistent with a longer lifetime of the perovskite/CrO_x film than the control film observed in the TRPL spectra (Figure 2c). For the perovskite films with a hole transport layer of Spiro-OMeTAD, more quenching is clearly observed (Figure 2b) and its carrier lifetime (τ₁ = 0.53 ns; τ₂ = 3.45 ns) is shorter than the control sample (τ₁ = 0.70 ns; τ₂ = 6.01 ns) (Figure 2c). It is revealed that CrO_x effectively enhances the photogenerated hole

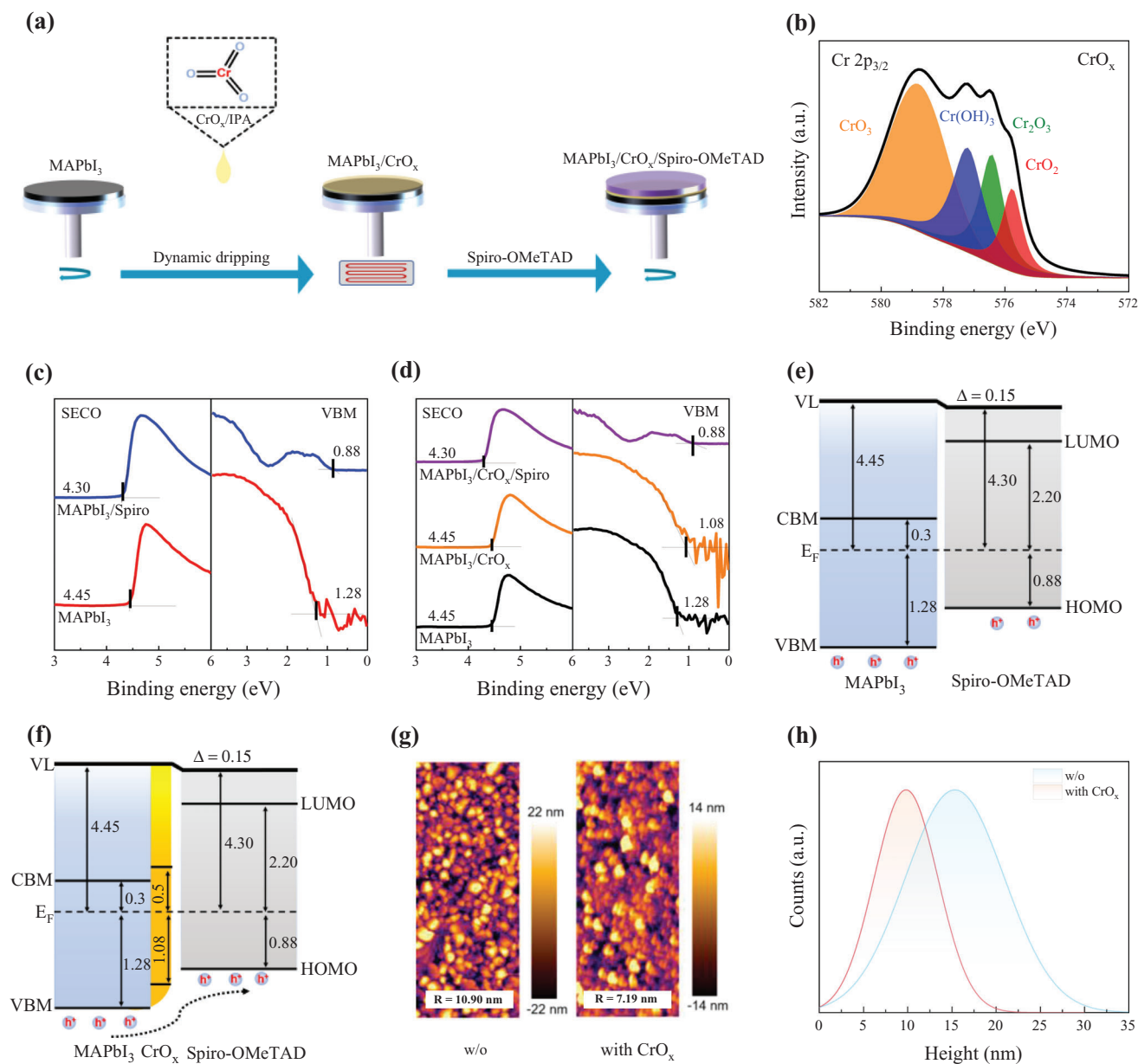


Figure 1. a) Schematics of fabrication processes of a MAPbI₃/CrO_x/Spiro-OMeTAD heterojunction. b) XPS Cr 2p_{3/2} core level spectra of CrO_x film. UPS-derived secondary electron cutoff regions and frontier electronic structure regions of c) MAPbI₃/Spiro-OMeTAD and d) MAPbI₃/CrO_x/Spiro-OMeTAD, respectively. e,f) Corresponding energy level alignments. g) Surface morphologies of MAPbI₃ films with and without CrO_x. h) Surface height histograms derived from the AFM images.

transfer from perovskite to Spiro-OMeTAD, reducing interface charge recombination at the hole-selective heterojunction. We further use the equation of $\eta_i = (1 - \frac{PLQY_{Per/HTL}}{PLQY_{Per}})^{[39]}$ to quantify the hole transfer efficiency (η_i) between the perovskite and Spiro-OMeTAD. The photoluminescence quantum yields (PLQYs) for the MAPbI₃ and MAPbI₃/CrO_x are 0.73% and 0.91%, respectively, and the PLQY values for the MAPbI₃/Spiro-OMeTAD and MAPbI₃/CrO_x/Spiro-OMeTAD are 0.22% and 0.02%, respectively (Figure 2d). The calculated η_i significantly increases from 69.87% to 97.80% at the heterojunction after inserting CrO_x.

We fabricate n-i-p planar PSCs with a device architecture of ITO/SnO₂/perovskite/CrO_x/Spiro-OMeTAD/Ag using MAPbI₃ displayed in Figure 3a. The dependence of the device PCE on the CrO_x layer thickness is carefully evaluated, and the optimal thickness that produces the champion device is 8 nm (Figures S4,S5; Table S2, Supporting Information). Figure 3b shows the current density-voltage (*J*-*V*) curves of the devices under a simulated AM 1.5 G light illumination at 100 Mw cm⁻². The control device has a typical PCE of 18.46% with an open-circuit voltage (*V*_{oc}) of 1.077 V, a short current density (*J*_{sc}) of 23.16 mA cm⁻² and a fill factor (FF) of 74%. In striking contrast, the champion device with

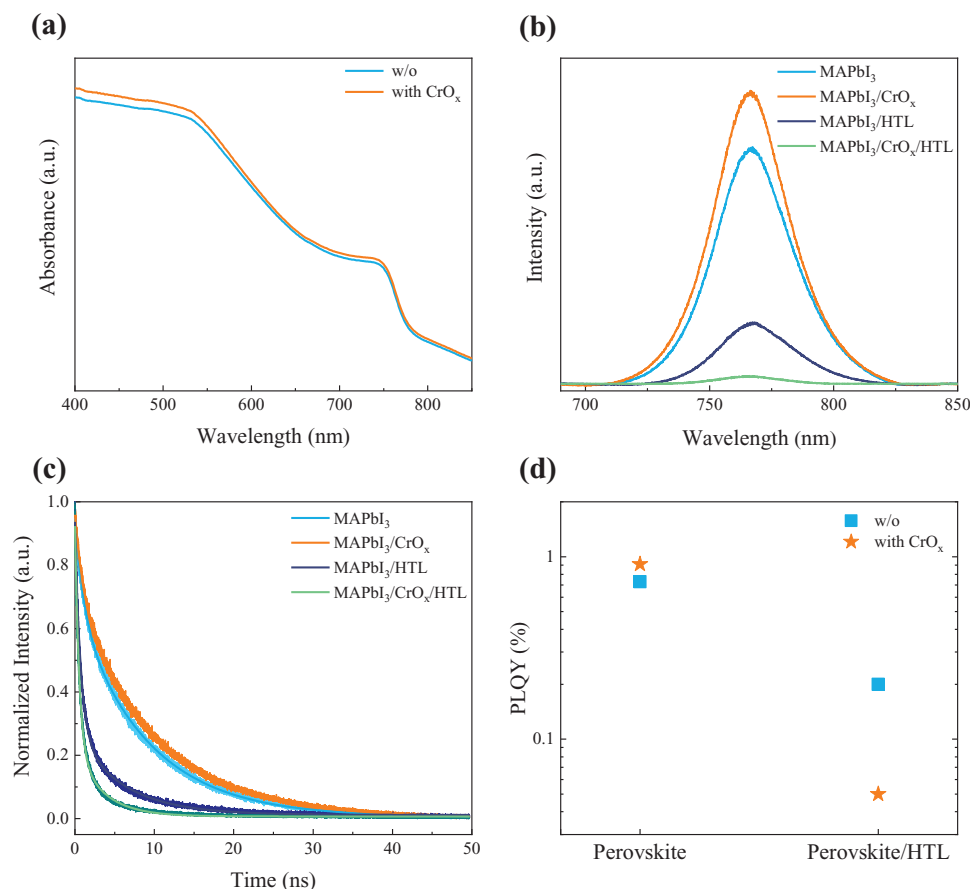


Figure 2. a) UV-vis absorption spectra of the perovskite films with and without CrO_x. b) Steady-state PL spectra, and c) Time-resolved PL decays. d) PLQY results.

CrO_x yields a remarkably improved PCE of 21.21% with a higher V_{oc} of 1.161 V, J_{sc} of 23.61 mA cm⁻² and FF of 77.39%. The obtained efficiencies are among the highest PCEs for polycrystalline MAPbI₃ based n-i-p planar PSCs reported to date (Figure 3c; Table S3, Supporting Information). **Table 1** summarizes the corresponding photovoltaic parameters of the devices for comparison.

We then characterize external quantum efficiency (EQE) spectra and the integrated photocurrent densities (22.90 mA cm⁻² for the device with CrO_x, 22.10 mA cm⁻² for the control device) closely agree with J_{sc} in the J - V curves (Figure 3d). The distinct difference in performance between the modified device and the control device is attributed to the improvement of all photovoltaic parameters including V_{oc} , J_{sc} , and FF. The statistical charts from the various batches in Figure 3e,f and Figure S6 (Supporting Information) show good reproducibility of the devices. We further investigate the stability of the device with CrO_x. The modified device has a stabilized photocurrent density of 22.35 mA cm⁻² and a stabilized power output of 21.01% at continuous operation (AM 1.5 G illumination) at the maximum power point for 300 s (Figure 3g). Under ambient air in 60% relative humidity at room temperature, the unencapsulated device with CrO_x retains 90% of its initial efficiency after up to 500 h storage, whereas the control device has only 10% of its initial PCE left (Figure 3h). The enhanced stability can be ascribed to the reduced perovskite surface defects and the increased hydrophobicity of the perovskite film coated

with CrO_x as the water contact angle largely increases from 44° to 87°. These results indicate that the CrO_x not only boosts the hole transport across the heterojunction, but also functions as a self-encapsulation layer to impede the attack of moisture on the underlying perovskite film and the penetrability of iodine ion into Spiro-OMeTAD.

To obtain more insight on the improved performance of our PSCs, we carry out the capacitance-voltage (C - V) curves to extract the built-in potential (V_{bi}) of the devices according to the Mott-Schottky equation:^[40] $\frac{1}{C^2} = \frac{2(V_{bi}-V)}{A^2 \epsilon \epsilon_0 N_A}$, where A is device area, N_A is charge carrier density, ϵ_0 is vacuum permittivity, and ϵ is relative permittivity. A higher V_{bi} of 1.03 V for the modified device is observed than 0.96 V for the control device, which is in accordance with the observed V_{oc} enhancement (Figure 4a). We ascribe the increased flat band potential to the reduced VBM-HOMO energy offset between the perovskite and Spiro-OMeTAD that diminishes thermionic losses for collecting holes at the heterojunction and thus reduces the device energy loss. We then estimate charge trap density and mobility using the space-charge-limited current (SCLC) method.^[41] As determined from the dark J - V curves of hole-only device with a structure of ITO/PTAA/MAPbI₃/CrO_x/Spiro-OMeTAD/Ag (Figure 4b), the calculated hole trap density decreases from 9.04×10^{15} cm⁻³ for the control device to 4.52×10^{15} cm⁻³ for the modified device, and the corresponding hole mobility increases from 1.12×10^{-3}

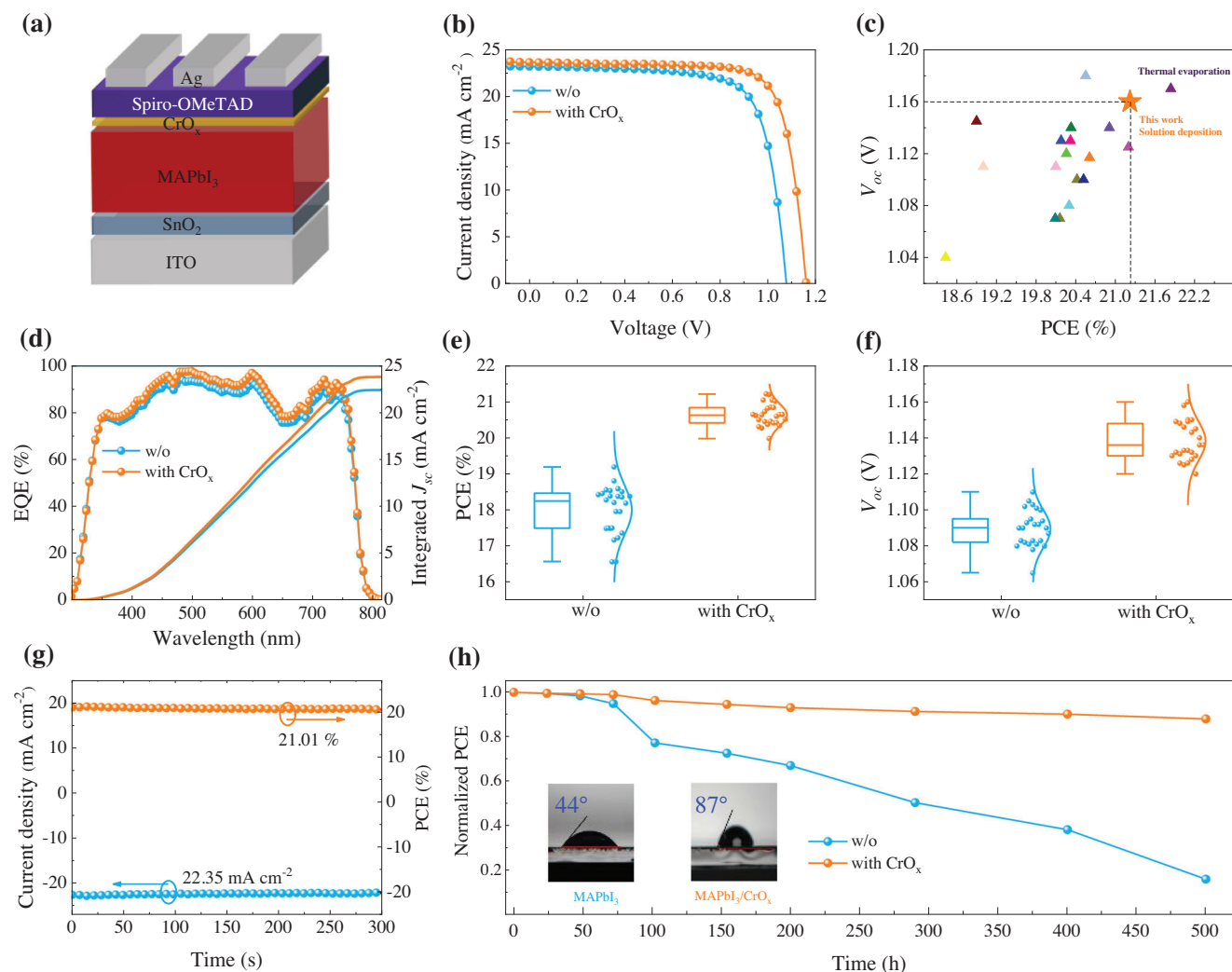


Figure 3. a) Device architecture of n-i-p planar PSCs. b) J - V curves of the control and device with CrO_x under reverse scan. c) Literature survey of recent achievements on V_{oc} and PCE of polycrystalline MAPbI_3 based n-i-p PSCs. d) EQE spectra and integrated photocurrent density. Statistics of e) PCE and f) V_{oc} of the devices. g) Steady-state photocurrent density and power output at the maximal power point. h) Comparison of normalized efficiency decay of unencapsulated PSCs as a function of storage time in ambient air with 60% relative humidity at room temperature. Insert represents the water angles of perovskite films with and without CrO_x .

Table 1. Photovoltaic parameters of the PSCs with and without CrO_x under reverse scan.

CrO_x	V_{oc} [V]	J_{sc} [mA cm^{-2}]	FF [%]	PCE [%]
w/o	1.077	23.16	74.00	18.46
with	1.161	23.61	77.39	21.21

to $5.60 \times 10^{-3} \text{ cm}^2 \text{ V}^{-1} \text{ s}^{-1}$. These results demonstrate that the defect density is greatly reduced and the charge transport is significantly improved across the perovskite/ CrO_x /Spiro-OMeTAD heterojunction. We also characterize the dark J - V curves of the full PSC device (Figure 4c). Both the leakage current at negative bias and the ideality factor (m) at positive bias of the modified device are smaller than those of the control device, suggesting suppressed nonradiative recombination. This is in agreement with

the increased recombination resistance (R_{rec}) fitted in the electrical impedance spectroscopy (EIS) in Figure 4d and Table S4 (Supporting Information).

To further elucidate the charge recombination mechanisms of the improved devices, we provide the light intensity (P) – dependent V_{oc} and J_{sc} , as displayed in Figure 4e,f, respectively. The slope of the dependence of V_{oc} versus P is applied to evaluate the degree of trap-assisted recombination via the equation:^[42] $V_{oc} = \frac{nKT}{q \ln(P)}$, where K is Boltzmann constant and T is absolute temperature. Compared with 1.91 KT q^{-1} for the control device, the slope of the device with CrO_x decreases to 1.66 KT q^{-1} , revealing that the trap-assisted recombination is effectively suppressed due to the reduced defect density. The relationship between J_{sc} and P can be expressed by $J_{sc} \propto P^\alpha$, where the exponential factor α represents the extent of biomolecular recombination.^[43] The extracted α of the modified device increases to 0.99 compared to 0.96 of the control device, indicating approximately

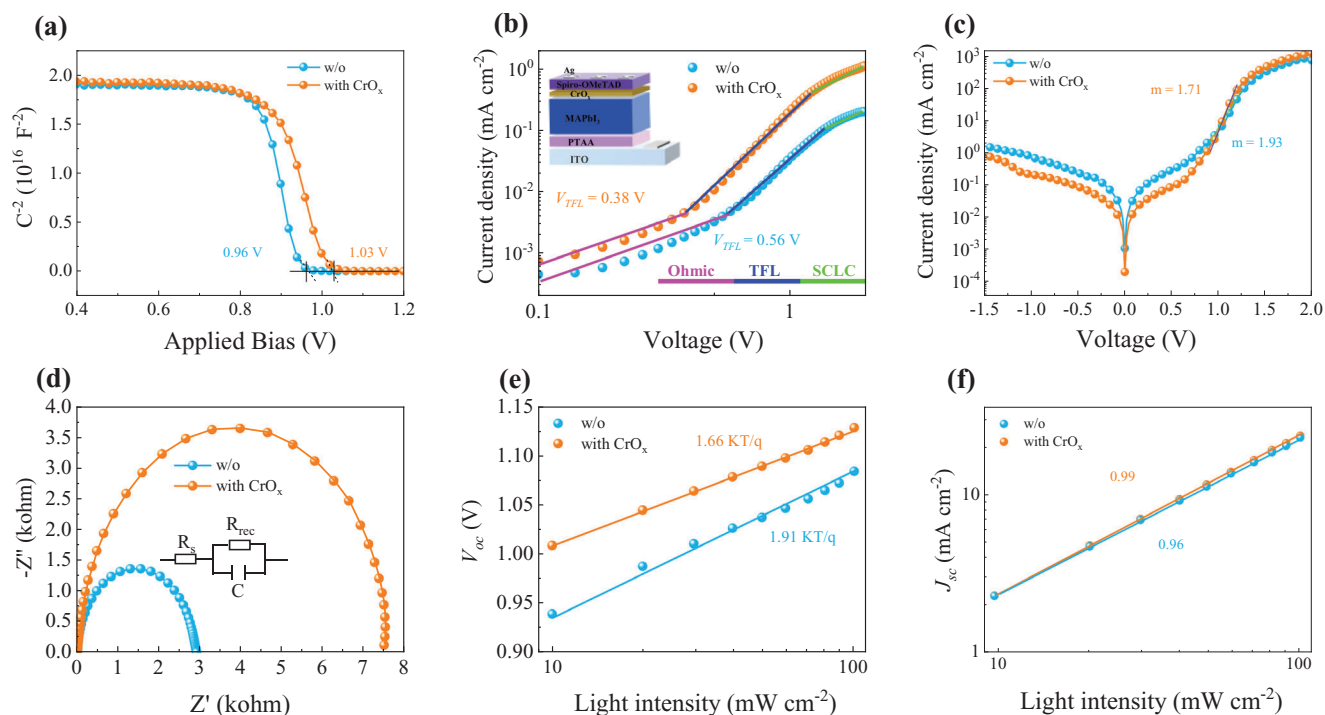


Figure 4. a) Mott–Schottky plots of PSCs. b) Dark J – V curves of hole-only devices. c) Dark J – V characteristics of PSCs. The ideality factor (m) is extracted from the diffusion-dominated current region according to the equation of $m = (\frac{kT}{q} \frac{d \ln J}{dV})^{-1}$.^[46] d) EIS Nyquist plots. e) Dependence of V_{oc} on light intensity and f) Dependence of J_{sc} on light intensity of PSCs.

a minimal interface charge recombination at the contact between perovskite and Spiro-OMeTAD after inserting CrO_x owing to the diminished VBM-HOMO offset and the improved hole extraction capability from perovskite to Spiro-OMeTAD. Notably, this is different from the formation of an interface dipole at the perovskite/thermally-evaporated molybdenum trioxide interface that reinforces the built-in field and prevents the photo-generated charges from recombining.^[37] The above results suggest that the perovskite/ CrO_x /Spiro-OMeTAD heterojunction effectively suppresses the nonradiative recombination in the PSCs, leading to a better hole transport. Additionally, it is expected that the CrO_x also acts as a charge generation layer due to spontaneous charge transfer from intrinsic defect states in oxides via thermal diffusion and the internal electric-field at the CrO_x /Spiro-OMeTAD interface.^[44,45] The generated holes from CrO_x inject into the neighboring Spiro-OMeTAD, which synchronously promotes the performance of the device.

3. Conclusion

In summary, we have demonstrated the roles of perovskite/ CrO_x /Spiro-MeTAD hole-selective heterojunction in developing high performance n–i–p planar PSCs. The solution-processed CrO_x composes multivalence state oxide complexes. The perovskite/ CrO_x /Spiro-MeTAD heterojunction not only effectively reduces the defect sites via a redox shuttle at the perovskite contact, but also decreases VBM-HOMO offset between perovskite and Spiro-OMeTAD. These result in diminishing thermionic losses for collecting holes at the

heterojunction, which thus promotes charge transport, and simultaneously suppresses both defect-assisted recombination and interface carrier recombination. As a result, we successfully achieve a PSC with a significantly improved PCE of 21.21% compared to 18.46% of the control device. Our efficiency is among the highest PCEs for polycrystalline MAPbI_3 based n–i–p planar PSCs reported to date. These findings of this work provide new insight into the improved performance of the PSCs via constructing highly efficient charge-selective heterojunctions.

4. Experimental Section

Materials: Lead iodide (PbI_2 , 99.99%), 2,2',7,7'-Tetrakis[N,N -di(4-methoxyphenyl)amino]-9,9'-spirobifluorene (Spiro-OMeTAD, 99.8%), bis(trifluoromethanesulfonyl)imide lithium (Li-TFSI, 99.95%), and tert-butylpyridine (tBP, 96%) were received from Polymer Light Technology Corp. Methylammonium iodide (MAI, 99.5%) was provided by Greatcell Solar Ltd. Stannic oxide (SnO_2) colloid precursor (15% in H_2O colloidal dispersion) and chromium trioxide powder (99.99%) were purchased from Alfa Aesar. N,N -Dimethylformamide (DMF, 99.8%), dimethyl sulfoxide (DMSO, 99.8%), isopropyl alcohol (IPA, 99.5%), acetonitrile, and chlorobenzene (CB, 99.5%) were obtained from Sigma–Aldrich. All materials were used as received.

Device Fabrication and Characterizations: Indium tin oxide (ITO)-coated glasses were washed by sequentially sonicating in deionized water, acetone, and ethanol for 30 min each step. The dried ITO was treated by UV–ozone for 20 min before use. The SnO_2 colloid precursor was diluted using ultrapure water (1:6 in volume ratio) and then spin-coated on the ITO at 3000 rpm for 30 s, and was annealed on a hotplate at 150 °C for 30 min in air. The MAPbI_3 perovskite precursor was prepared by dissolving 497.8 mg PbI_2 and 159.0 mg MAI in the mixed solvent of DMF/DMSO

(750 μL :85 μL). The perovskite film was spin-coated on the electron transport layer SnO_2 at 4000 rpm for 30 s in a N_2 -filled glove-box. 120 μL CB was dripped at the center of the film after 7 s spin coating, and the perovskite film was annealed at 105 $^\circ\text{C}$ for 10 mins. The filtered CrO_x solution in IPA with the different concentrations was spin-coated on the perovskite film at 6000 rpm for 30 s, following by 100 $^\circ\text{C}$ annealing for 10 min. The hole transport layer spiro-OMeTAD (73 mg spiro-OMeTAD in 28.8 μL tBP and 17.5 μL Li-TFSI solution with 520 mg ML^{-1} in acetonitrile) was deposited on the perovskite film via spin-coating at 4000 rpm for 30 s. Finally, a 100 nm silver layer was deposited by thermal evaporation with a mask at a pressure of 10^{-6} mbar. The J - V curves of the devices were measured in the N_2 -filled glovebox using a Keithley 2400 system under a solar simulator (SS-F5-3A, Enlitech). The light intensity (100 mW cm^{-2}) was calibrated by a certified standard silicon solar cell with KG-5 filter (SRC-2020, Enlitech). The EQE spectra were recorded by QE-R system (Enlitech). The capacitance-voltage curve was conducted by an impedance spectroscopy (PGSTAT302N, Autolab). The EIS measurement was performed via a precision impedance analyzer (Agilent 4294A) under a bias of 1 V.

Film Characterizations: The surface roughness of the film was measured by AFM (Asylum Research, Oxford). The XRD patterns were recorded using PANalytical X-ray diffractometer with $\text{Cu K}\alpha$ radiation. The UV-vis absorption spectra were collected by UV/vis/NIR spectrometer (TU-1901). The steady-state PL spectra were recorded with a fluorescence spectrometer (PerkinElmer LS 55) using a 470 nm excitation light source. The time-resolved PL decay was measured via a time-corrected single photon counting system at an excitation wavelength of 373 nm. The PLQY was collected on a fluorometer equipped with an integrating sphere at a wavelength of 470 nm (FS-5, Edinburgh).

Photoelectron Spectroscopy Measurements: UPS/XPS measurements were performed in an ultrahigh vacuum surface analysis system equipped with a fast entry load-lock, a transfer chamber, a preparation chamber and an analysis chamber with a base pressure of 10^{-10} mbar. A Scienta R3000 spectrometer was equipped to detect the photoelectron kinetics. UPS was employed with the He I 21.22 eV as the excitation source and an energy resolution of 50 meV. The work function and VBM were derived from the secondary electron cutoff and the frontier edge of the occupied density states, respectively. The precise VBM position of the perovskite film was determined in a logarithmic intensity scale due to its strong band dispersion, and the VBM position of Spiro-OMeTAD was determined in a linear intensity scale. XPS was carried out with a monochromatic Al $\text{K}\alpha$ 1486.6 eV as the excitation source. All recorded spectra were calibrated by referring to the Fermi level edge and Au 4f_{7/2} position of the Ar^+ ion sputter-cleaned Au film.

Supporting Information

Supporting Information is available from the Wiley Online Library or from the author.

Acknowledgements

This work was supported by the National Science Foundation of China grant (21875067), Shanghai Science and Technology Innovation Action Plan (22ZR1418900), the Fundamental Research Funds for the Central Universities, Shanghai Rising-Star (19QA1403100), and East China Normal University (ECNU) Multifunctional Platform for Innovation. L. Ding thanks the open research fund of Songshan Lake Materials Laboratory (2021SLABFK02), the National Key Research and Development Program of China (2017YFA0206600), and the National Natural Science Foundation of China (51922032, 21961160720).

Conflict of Interest

The authors declare no conflict of interest.

Data Availability Statement

The data that support the findings of this study are available from the corresponding author upon reasonable request.

Keywords

charge transport, efficiency, hole-selective heterojunction, nonradiative recombination, perovskite solar cells

Received: July 21, 2022

Revised: August 9, 2022

Published online:

- [1] Z. Xiao, C. Bi, Y. Shao, Q. Dong, Q. Wang, Y. Yuan, C. Wang, Y. Gao, J. Huang, *Energy Environ. Sci.* **2014**, 7, 2619.
- [2] A. A. Zhumekenov, M. I. Saidaminov, M. A. Haque, E. Alarousu, S. P. Sarmah, B. Murali, I. Dursun, X. Miao, A. L. Abdelhady, T. Wu, O. F. Mohammed, O. M. Bakr, *ACS Energy Lett.* **2016**, 1, 32.
- [3] L. Zhang, X. Pan, L. Liu, L. Ding, *J. Semicond.* **2022**, 43, 030203.
- [4] N. G. Park, *J. Phys. Chem. Lett.* **2013**, 4, 2423.
- [5] D. Ju, Y. Dang, Z. Zhu, H. Liu, C. Chueh, X. Li, L. Wang, X. Hu, A. K. Y. Jen, X. Tao, *Chem. Mater.* **2018**, 30, 1556.
- [6] C. S. Ponseca Jr., T. J. Savenije, M. Abdellah, K. Zheng, A. Yartsev, T. Pascher, T. Harlang, P. Chabera, T. Pullerits, A. Stepanov, J. P. Wolf, V. Sundstrom, *J. Am. Chem. Soc.* **2014**, 136, 5189.
- [7] Y. Zhou, J. Chen, O. M. Bakr, O. F. Mohammed, *ACS Energy Lett.* **2021**, 6, 739.
- [8] L. Mei, H. Mu, L. Zhu, S. Lin, L. Zhang, L. Ding, *J. Semicond.* **2022**, 43, 040203.
- [9] K. Akihiro, T. Kenjiro, S. Yasuo, M. Tsutomu, *J. Am. Chem. Soc.* **2009**, 131, 6050.
- [10] H. Min, D. Lee, J. Kim, G. Kim, K. S. Lee, J. Kim, M. J. Paik, Y. K. Kim, K. S. Kim, M. G. Kim, T. J. Shin, S. I. Seok, *Nature* **2021**, 598, 444.
- [11] M. Cheng, C. Zuo, Y. Wu, Z. Li, B. Xu, Y. Hua, L. Ding, *Sci. Bull.* **2020**, 65, 1237.
- [12] D. He, T. Zhou, B. Liu, L. Bai, W. Wang, H. Yuan, C. Xu, Q. Song, D. Lee, Z. Zang, L. Ding, J. Chen, *EcoMat* **2021**, 4, e12158.
- [13] Y. Liu, B. Dong, A. Hagfeldt, J. Luo, M. Graetzel, *Smart Mat.* **2021**, 2, 33.
- [14] S. Xiong, Z. Hou, W. Dong, D. Li, J. Yang, R. Bai, Y. Wu, D. Li, H. Wu, Z. Ma, J. Xu, X. Liu, Q. Bao, *Adv. Energy Mater.* **2021**, 11, 2101394.
- [15] J. Warby, F. Zu, S. Zeiske, E. Gutierrez Partida, L. Frohloff, S. Kahmann, K. Frohna, E. Mosconi, E. Radicchi, F. Lang, S. Shah, F. Peña-Camargo, H. Hempel, T. Unold, N. Koch, A. Armin, F. De Angelis, S. D. Stranks, D. Neher, M. Stollerfoht, *Adv. Energy Mater.* **2022**, 12, 2103567.
- [16] P. Caprioglio, M. Stollerfoht, C. M. Wolff, T. Unold, B. Rech, S. Albrecht, D. Neher, *Adv. Energy Mater.* **2019**, 9, 1901631.
- [17] P. Schulz, E. Edri, S. Kirmayer, G. Hodes, D. Cahen, A. Kahn, *Energy Environ. Sci.* **2014**, 7, 1377.
- [18] F. Zhang, H. L. Smith, A. Kahn, *Appl. Phys. Rev.* **2021**, 8, 041301.
- [19] P. Schulz, L. L. Whittaker Brooks, B. A. MacLeod, D. C. Olson, Y. Loo, A. Kahn, *Adv. Mater. Interfaces* **2015**, 2, 1400532.
- [20] Z. Hawash, L. K. Ono, Y. Qi, *Adv. Mater. Interfaces* **2017**, 5, 1700623.
- [21] J. M. Ball, M. M. Lee, A. Hey, H. J. Snaith, *Energy Environ. Sci.* **2013**, 6, 1739.
- [22] L. Liang, H. Luo, J. Hu, H. Li, P. Gao, *Adv. Energy Mater.* **2020**, 10, 2000197.
- [23] M. Li, T. Sun, J. Shao, Y. Wang, J. Hu, Y. Zhong, *Nano Energy* **2021**, 79, 105462.

- [24] M. Cha, P. Da, J. Wang, W. Wang, Z. Chen, F. Xiu, G. Zheng, Z. S. Wang, *J. Am. Chem. Soc.* **2016**, *138*, 8581.
- [25] P. Guo, H. Zhu, W. Zhao, C. Liu, L. Zhu, Q. Ye, N. Jia, H. Wang, X. Zhang, W. Huang, V. A. Vinokurov, E. Ivanov, D. Shchukin, D. Harvey, J. M. Ulloa, A. Hierro, H. Wang, *Adv. Mater.* **2021**, *33*, 2101590.
- [26] B. Zhao, X. Yan, T. Zhang, X. Ma, C. Liu, H. Liu, K. Yan, Y. Chen, X. Li, *ACS Appl. Mater. Interfaces* **2020**, *12*, 9300.
- [27] J. Carrillo, A. Guerrero, S. Rahimnejad, O. Almora, I. Zarazua, E. Mas Marza, J. Bisquert, G. Garcia Belmonte, *Adv. Energy Mater.* **2016**, *6*, 1502246.
- [28] H. Guo, Y. Fang, H. B. Cheng, J. Wu, Y. Lei, S. Wang, X. Li, Y. Dai, W. Xiang, D. J. Xue, Y. Lin, A. Hagfeldt, *Angew. Chem., Int. Ed.* **2022**, e202204148.
- [29] W. Deng, X. Liang, P. S. Kubiak, P. J. Cameron, *Adv. Energy Mater.* **2018**, *8*, 1701544.
- [30] N. K. Noel, S. N. Habisreutinger, A. Pellaroque, F. Pulvirenti, B. Wenger, F. Zhang, Y. Lin, O. G. Reid, J. Leisen, Y. Zhang, S. Barlow, S. R. Marder, A. Kahn, H. J. Snaith, C. B. Arnold, B. P. Rand, *Energy Environ. Sci.* **2019**, *12*, 3063.
- [31] M. Kaltenbrunner, G. Adam, E. D. Glowacki, M. Drack, R. Schwodiauer, L. Leonat, D. H. Apaydin, H. Groiss, M. C. Scharber, M. S. White, N. S. Sariciftci, S. Bauer, *Nat. Mater.* **2015**, *14*, 1032.
- [32] T. H. Schloemer, J. A. Raiford, T. S. Gehan, T. Moot, S. Nanayakkara, S. P. Harvey, R. C. Bramante, S. Dunfield, A. E. Louks, A. E. Maughan, L. Bliss, M. D. McGehee, M. F. A. M. van Hest, M. O. Reese, S. F. Bent, J. J. Berry, J. M. Luther, A. Sellinger, *ACS Energy Lett.* **2020**, *5*, 2349.
- [33] I. S. Kim, A. B. F. Martinson, *J. Mater. Chem. A* **2015**, *3*, 20092.
- [34] Y. H. Lee, J. Luo, M. K. Son, P. Gao, K. T. Cho, J. Seo, S. M. Zakeeruddin, M. Gratzel, M. K. Nazeeruddin, *Adv. Mater.* **2016**, *28*, 3966.
- [35] W. Lin, W. Wu, Z. Liu, K. Qiu, L. Cai, Z. Yao, B. Ai, Z. Liang, H. Shen, *ACS Appl. Mater. Interfaces* **2018**, *10*, 13645.
- [36] W. Ligang, Z. Huanping, H. Junnan, H. Bolong, S. Mingzi, D. Bowei, Z. Guanghaojie, H. Yuan, C. Yihua, L. Liang, X. Ziqi, L. Nengxu, L. Zheng, C. Qi, S. Ling-Dong, Y. ChunHua, *Science* **2019**, *363*, 265.
- [37] F. Wang, Y. Zhang, M. Yang, D. Han, L. Yang, L. Fan, Y. Sui, Y. Sun, X. Liu, X. Meng, J. Yang, *Adv. Funct. Mater.* **2020**, *31*, 2008052.
- [38] W. Zhao, Z. Yao, F. Yu, D. Yang, S. F. Liu, *Adv. Sci.* **2018**, *5*, 1700131.
- [39] V. Ferguson, B. Li, M. O. Tas, T. Webb, M. T. Sajjad, S. A. J. Thomson, Z. Wu, Y. Shen, G. Shao, J. V. Anguita, S. R. P. Silva, W. Zhang, *Adv. Mater. Interfaces* **2020**, *7*, 2001121.
- [40] O. Almora, C. Aranda, E. M. Marza, G. Garcia-Belmonte, *Appl. Phys. Lett.* **2016**, *109*, 173903.
- [41] M. Sajedi Alvar, P. W. M. Blom, G. A. H. Wetzelaer, *Nat. Commun.* **2020**, *11*, 4023.
- [42] M. Bernechea, N. C. Miller, G. Xercavins, D. So, A. Stavrinadis, G. Konstantatos, *Nat. Photonics* **2016**, *10*, 521.
- [43] L. Xie, A. N. Cho, N. G. Park, K. Kim, *ACS Appl. Mater. Interfaces* **2018**, *10*, 9390.
- [44] Q. Y. Bao, J. P. Yang, Y. Q. Li, J. X. Tang, *Appl. Phys. Lett.* **2010**, *97*, 063303.
- [45] J. Yang, Y. Xiao, Y. Deng, S. Duhm, N. Ueno, S. Lee, Y. Li, J. Tang, *Adv. Funct. Mater.* **2012**, *22*, 600.
- [46] S. Xiong, Z. Hou, S. Zou, X. Lu, J. Yang, T. Hao, Z. Zhou, J. Xu, Y. Zeng, W. Xiao, W. Dong, D. Li, X. Wang, Z. Hu, L. Sun, Y. Wu, X. Liu, L. Ding, Z. Sun, M. Fahlman, Q. Bao, *Joule* **2021**, *5*, 467.